Pushing down the limit of NH_3 detection of graphene-based chemiresistive sensors through functionalization by thermally activated tetrazoles dimerization

Sonia Freddi,[a,b,#] Daniele Perilli,[c,#] Luca Vaghi,[c] Mauro Monti,[c] Antonio Papagni,[c] Cristiana Di Valentin,[c] Luigi Sangaletti[a,*]

[a] Surface Science and Spectroscopy lab @ I-Lamp, Department of Mathematics and Physics, Università Cattolica del Sacro Cuore, Via della Garzetta, 48 25123 Brescia, Italy

[b] Department of Chemistry, Division of Molecular Imaging and Photonics, KU Leuven, Celestijnenlaan 200F, 3001 Leuven, Belgium.

[c] Department of Materials Science, University of Milano-Bicocca, via Cozzi 55, 20125 Milano, Italy

[*]Corresponding author: luigi.sangaletti@unicatt.it

[#] S.F. and D.P. equally contributed to the manuscript

Abstract

An easy and cost-effective method is presented to functionalize graphene through thermally activated dimerization of 2,5-diaryltetrazoles. Consistently with the experimental spectroscopic results, theoretical calculations demonstrate that during the thermal treatment a dimerization process to tetrazine is energetically more favorable than covalent grafting. Since both the functionalization method by thermal activation and the use of tetrazoles have never been considered before to prepare graphene-based chemiresistors, this represents a promising approach to develop graphene-related sensing platforms. Five different 2,5-diaryltetrazoles have been tested here for the effective functionalization of low-defect graphene layers on silicon nitride. Based on these layers, an array of sensors has been prepared for testing upon ammonia exposure. The tests on the sensing performances clearly show a remarkable sensitivity to ammonia, extending the current range of ammonia detection with graphene-based chemiresistor down to the sub-ppm range, as results from a benchmarking with data available in the literature. Furthermore, all sensors perform better than bare graphene. Density functional theory (DFT) calculations, carried out on a model of the best performing layer of the array provided the theoretical framework to rationalize the sensing mechanism and disclose a dual role played by the tetrazine molecules, (i) acting as ammonia concentrators and (ii) mediating the electron transfer between ammonia and graphene.

Key words: graphene, gas sensor, ammonia, tetrazoles, tetrazines

Introduction

Highly sensitive gas sensing materials, as well as ammonia monitoring, are of great importance for several applications, including environmental pollutants detection, [1-3] food quality tracking, [4-6] and medical screening campaigns. [7-10]

Indeed, concentrations of ammonia higher than 10 ppb in the exhaled breath of a patient can be related to liver or kidney pathologies, [11] while regarding environmental monitoring, ammonia is the precursor of fine particulate (PM2,5 and PM10), which is very dangerous for human respiratory health. [12] Finally, spoiled food, especially cheese and meat, releases small quantities of ammonia. [13] Taking into account this information, it is clear why developing cheap and effective gas sensors to detect low ammonia concentrations would be a groundbreaking achievement for many fields.

Graphene is probably one of the most studied materials in recent years, due to its intrinsic remarkable properties, such as high in plane conductivity leading to a low electrical intrinsic noise, [14] its excellent chemical stability at room temperature, [15] and its high sensitivity to surface adsorption of gas molecules, [16] which make it a promising candidate for gas sensor development. Within the graphene family, graphene oxide (GO) or reduced graphene oxide (rGO) have been so far the most investigated for the development of gas sensors, since their highly defective nature is expected to favor the interaction with gas molecules, enhancing the sensor response. [17,18] Nevertheless, GO- and rGO-based gas sensors have some drawbacks, from the high production cost [19] to the irreversible recovery to the initial condition after gas exposure, which makes their sensing capability not reliable. [20]

Consequently, ad-hoc functionalization of pristine graphene has been recently explored as a methodology to enhance its sensing capability.[21,22] Graphene could be functionalized in several ways, including both covalent and non-covalent bonding,[23] and different experimental approaches could be followed for the functionalization: from single atoms (mostly boron or nitrogen) [24,25] to nanoparticles, [26,27] or organic molecules. [28,29]

In the present work an easy and low-cost small molecules functionalization method, based on tetrazoles chemistry, has been developed to functionalize pristine graphene layers, that have been successfully employed in ammonia gas sensing. In detail, different tetrazoles molecules in solution have been dropcasted on graphene layers that, after thermal activation in nitrogen atmosphere at 250 °C, have generated highly reactive nitrilimines. [30] What happens to

nitrilimines on the graphene surface is relevant to the present study. According to [31], a highly reactive nitrilimine species in the presence of defects and edges, could covalently graft on the graphene surface modulating its work function. However, the authors do not report what happens to the nitrilimine if the graphene layer does not present a high density of defects and therefore the nitrilimine does not covalently graft on graphene.

Nitrilimines species, generated from tetrazoles by either heat or UV-irradiation, are reactive towards a plethora of functional groups (Scheme 1) [32-34] and this reactivity has been successfully exploited for numerous applications, such as labeling and cross-linking of biological substrates, [35,36] polymers functionalization for explosive detection [37] and surface chemistry. [38]

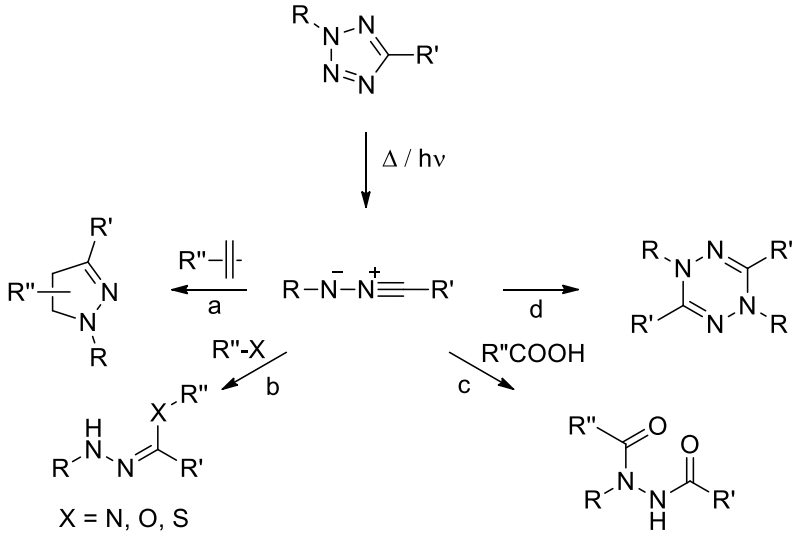

Scheme 1. Reactivity of nitrilimines. [32-34]

However, when no reactive counterpart is present and under determinate conditions, nitrilimines can self-react to form new entities by dimerization or oligomerization pathways. In particular, thermal treatment of 2,5-diaryltetrazoles in melt, yield, predominantly, *via* a head-to-tail mechanism, 1,3,4,6-tetraryltetrazines (Scheme 1, pathway d). [39]

On this basis, we tested five different 2,5-diaryltetrazoles (**1**-**5**, Figure 1) for the functionalization of low-defect graphene layer on silicon nitride and the prepared samples have then been simultaneously tested as gas sensors at room temperature, showing remarkable capability to track ammonia at low concentration, compared with results reported for chemiresistor graphene-based sensors to date.

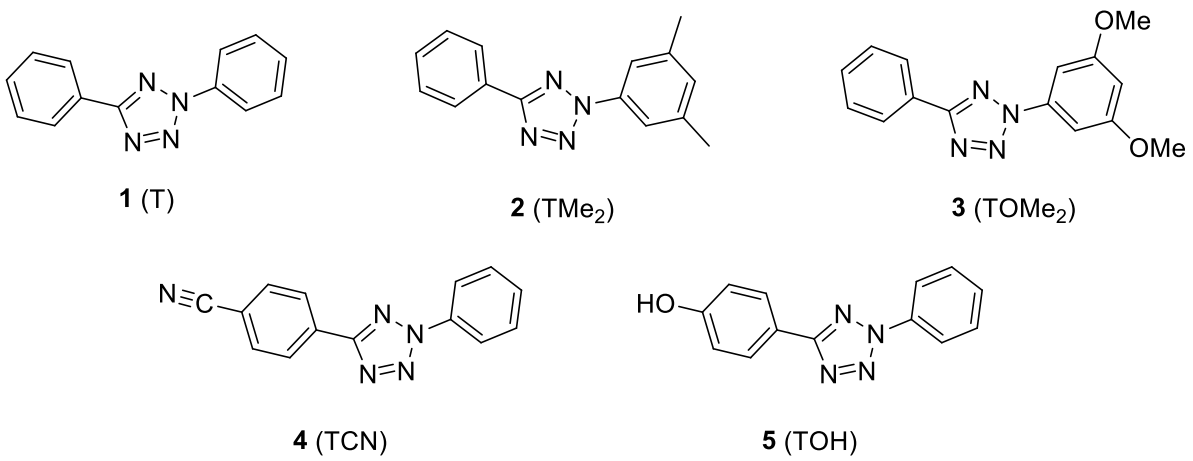

1 (T) **2** (TMe_2) **3** ($TOMe_2$)

4 (TCN) **5** (TOH)

Figure 1. Selected tetrazoles molecules for the functionalization of graphene:
1. T: 2,5-diphenyl-2H-tetrazole;
2. TMe_2: 2-(3,5-dimethylphenyl)-5-phenyl-2H-tetrazole;
3. $TOMe_2$: 2-(3,5-dimethoxyphenyl)-5-phenyl-2H-tetrazole;
4. TCN: 4-(2-phenyl-2H-tetrazole-5-yl)benzonitrile;
5. TOH: 4-(2-phenyl-2H-tetrazole-5-yl)phenol.

Theoretical calculations and spectroscopical analyses of the samples reveal that this remarkable sensing capability is given by the 1,3,4,6-tetraaryltetrazines on the graphene surface after the functionalization treatment, as the lack of defects and edges in the graphene layer hindered any potential cycloaddition reactions.

Results and Discussion

Synthesis of 2,5-diaryl-2*H*-tetrazoles 1-5

2,5-diaryl-2*H*-tetrazoles **1-5** were synthesized according to a reported procedure (Scheme 2). [40] The selected aldehyde reacted with tosylhydrazine in refluxing EtOH. The tosylhydrazone intermediate was not purified and treated with the diazonium salt of the suitable aniline to afford the expected 2,5-diaryl-2*H*-tetrazole.

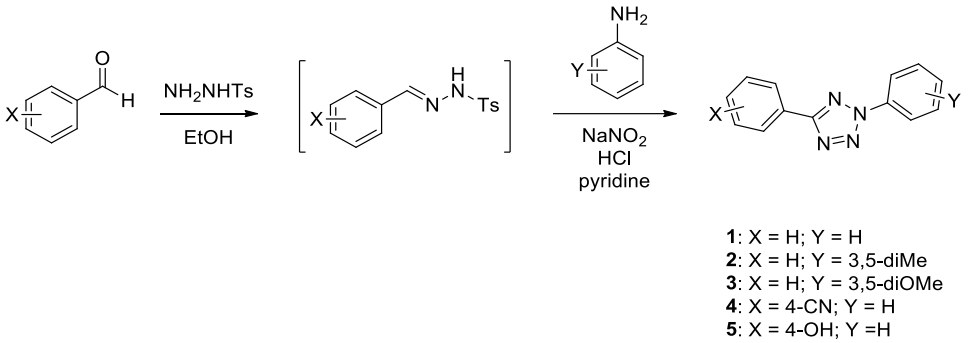

Scheme 2. Synthesis of **1-5**.

Grafting or Dimerization

Surface functionalization of Gr by grafting usually requires defective sites, such as undercoordinated C atoms located at edges and/or vacancies, which are more reactive and prompter to bind covalently to molecules.[31] For this reason, since defects in the graphene samples used in this work are relatively low (as will be discussed and proved below), we expect a low tendency to grafting.

In order to clarify the competition between grafting and dimerization to tetrazine, we performed an energetic analysis by calculating and comparing the DFT energies of reactants, intermediates, and products along the two possible reaction paths (as shown in Figure 2). In line with the experimental samples, we considered a perfect graphene monolayer, free from defects that may favor grafting. Moreover, among all the tetrazoles considered in this work, we chose the 1,3,4,6-tetraaryl-1,4-dihydro-1,2,4,5-tetrazine (TOH), as a case study, because of its remarkable sensing capability, as it will be disclosed later, and because its composition yields to an easier characterization analysis, especially as relates to XPS.

We started by virtually depositing two tetrazole molecules onto the Gr surface (Figure 3a). This model structure represents the system before any heat treatment, only after the solvent evaporation which leaves the molecular precursors adsorbed on the graphene surface.

Then, due to the thermal treatment, each adsorbed tetrazole decomposes and releases one N_2 molecule in the gas-phase by forming a nitrilimine intermediate (Figure 3b). Such a 1,3-dipolar compound presents a charge separation that makes it prone to react with other elements in the

environment. Here, two possible scenarios open up: 1) the formation of a pyrazoline compound through a 1,3-dipolar cycloaddition reaction (grafting, Figure 3c), or 2) the formation of a tetrazine compound through a dimerization reaction (Figure 3d). It is worth pointing out that even if the cycloaddition on graphene is reported to take place only on defective site, we calculated the reaction energy of a possible grafting in the areas of the graphene without defects, in line with the morphology of the experimental samples.

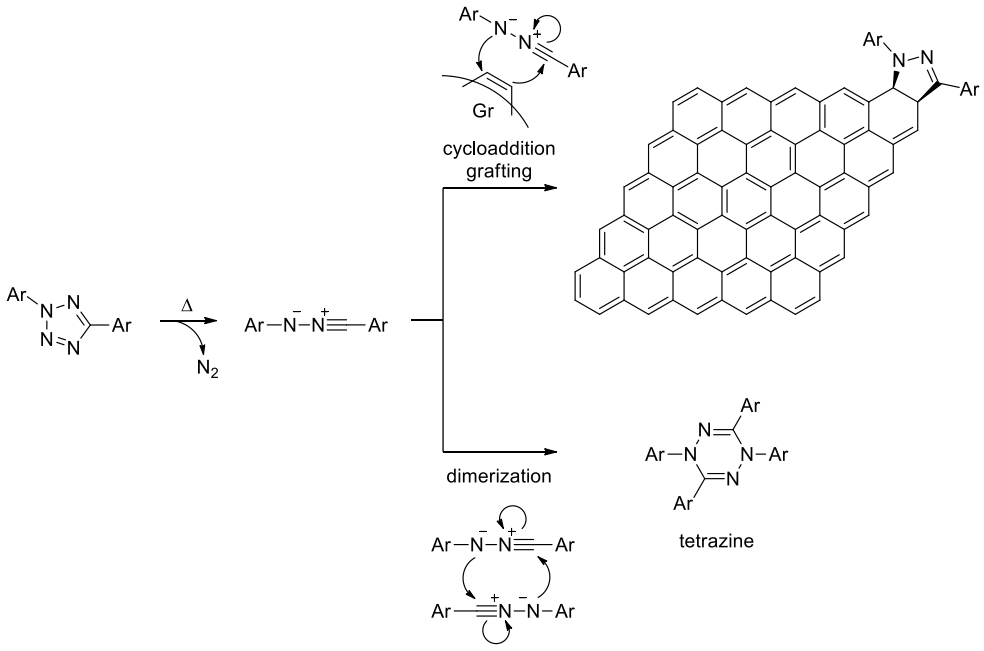

Figure 2. Competitive pathways of thermal generated nitrilimine from 2,5-diaryltetrazoles in presence of graphene layers.

As shown in Figure 4, the grafting is clearly more energetically expensive than the dimerization process (4.86 eV vs -0.19 eV with respect to the Gr-TOH(tetrazole).

The reason is that grafting requires the formation of covalent bonds between the adsorbed molecules and the Gr surface, leading to a disruption of the graphene sp^2 system. Indeed, as one can clearly see from the side view of Figure 2c, four C atoms become highly pyramidalized (two per molecule) due to the change of their hybridization from sp^2 to sp^3. This energy cost has been calculated to amount to ≈ 4.6 eV (≈ 2.3 eV per pyrazoline molecule), in good agreement with the energy difference of 5.05 eV between the two configurations.

On the contrary, in the case of the dimer formation, no rehybridization of the graphene C orbitals is required, which makes the process more energetically favorable.

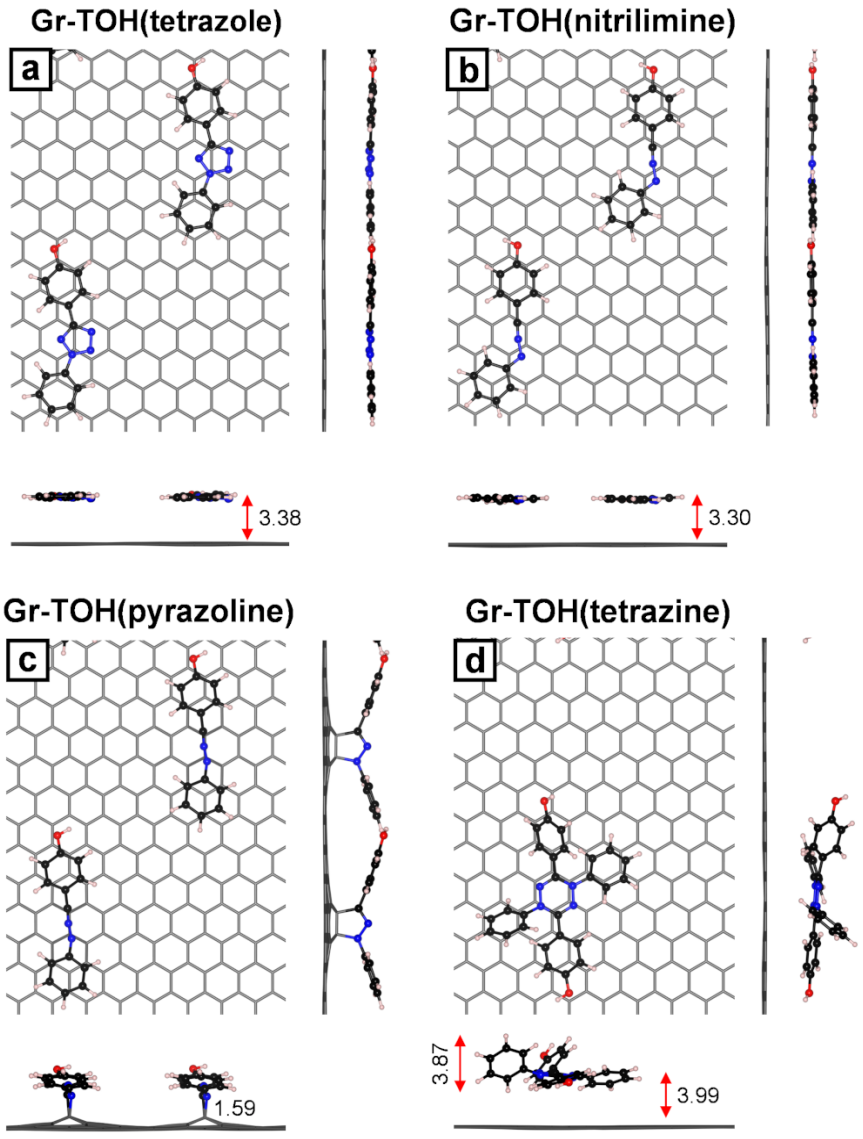

Figure 3: Ball-and-stick models (top and side views) for reagents, intermediates, and products along with the two possible grafting and dimerization processes (Figure 2). Color coding: C atoms in Gr are rendered in dark grey (stick representation); C, N, O, and H atoms in the adsorbed molecules are rendered in black, blue, red, and white, respectively (ball-and-stick representation). Distances are reported in Å.

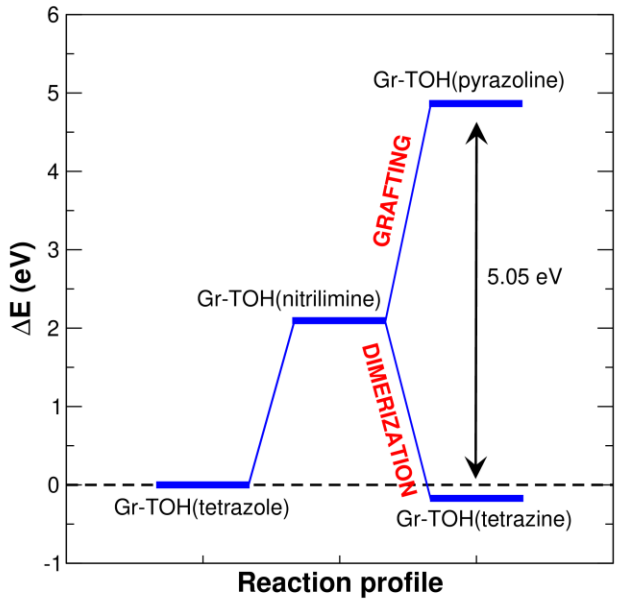

Figure 4: Energy profile for the grafting and dimerization processes. The first reaction step (which involves the release of N_2 in the gas-phase) is shared between the two mechanisms. The corresponding geometries are reported in Figure 3.

To summarize, based on our simulations, no evidence that grafting is energetically favored with respect to dimer formation has been found. Grafting could be a competitive process only if the graphene sample exhibits high defectivity, making it easier to form covalent bonds between the molecule and the surface. To support these conclusions, a thorough experimental characterization of the functionalized graphene samples has been carried out, through AFM, Raman, and XPS analysis.

AFM representative images collected on the sample are reported in Figure S1. All the functionalized samples present a homogeneous layer, except for the Gr-TCN case, where agglomerates, which are probably due to the possible reaction of nitrilimine with the CN triple bond. [41]

Representative Raman spectra of each sample are reported in Figure 5a. Starting from the pristine graphene (red spectrum) the G band, located at 1590 cm^{-1}, and the 2D band, located at 2649 cm^{-1}, are clearly present. The former band is ascribed to the C-C stretching of sp^2 hybridized carbon atoms in the graphene lattice, while the latter is a second order Raman scattering process, and it is related to the breathing mode of carbon atoms in the plane of

graphene.[42] In pristine graphene a feature around 1445 cm^{-1} is detectable. This band has also been reported by A. Gupta et al. [43] for graphene layers on Si/SiO_2 and ascribed to disorder-induced first order scattering. After an extensive Raman data analysis on different pristine graphene samples, we found that in most cases this band is present in pristine graphene samples. Therefore, we tentatively ascribe it to the contribution of the graphene layer (in agreement with ref. 43), assuming that the deposition of the tetrazole overlayer may contribute to a quenching of its intensity.

The feature detected around 1340 cm^{-1} likely has a two-fold origin: indeed, the silicon nitride substrate has a band in the same position,[44] but also the D-band related to defects in graphene, and in particular to the formation of sp^3 hybridization of some graphene C atoms upon the covalent attachment of a molecule, was reported around 1330 cm^{-1}.[42] The I_D/I_G ratio in the pristine graphene spectrum is quite low (i.e. 0.15±0.02), and, taking into account that this value is probably overestimated due to the silicon nitride contribution, it is possible to conclude that the monolayer graphene is not highly defective. Regarding the treated samples, G and 2D bands are always present, while no increase in the D-band is observed when comparing with the Gr pristine sample. This confirms what has been theoretically predicted, i.e. that the grafting process does not occur, or it occurs with very low efficiency, during the thermal treatment.

In order to verify the successful dimerization and consequent physisorption of the tetrazine on the graphene layer, extensive XPS analysis has been performed on the TOH system, due to its already mentioned remarkable sensing performances, focusing mainly on the N 1s peak contribution. In details, a powder of TOH, which has undergone the same thermal treatment as all samples, was directly dropcasted on a graphene on silicon/silicon dioxide substrate. This substrate was chosen to avoid any contribution of nitrogen coming from the substrate, thereby focusing only on the contribution coming from the annealed powder, mainly constituted by the tetrazine moiety. Figure 5b displays the N 1s core level spectrum, collected on the TOH powder on graphene on Si/SiO_2, which exhibits mainly two peaks: one around BE = 399.5 eV, ascribable to N-N-C bond, and the other related to the N-N=C bond at about BE = 401 eV. [45] Both peaks are consistent with the presence of tetrazine.

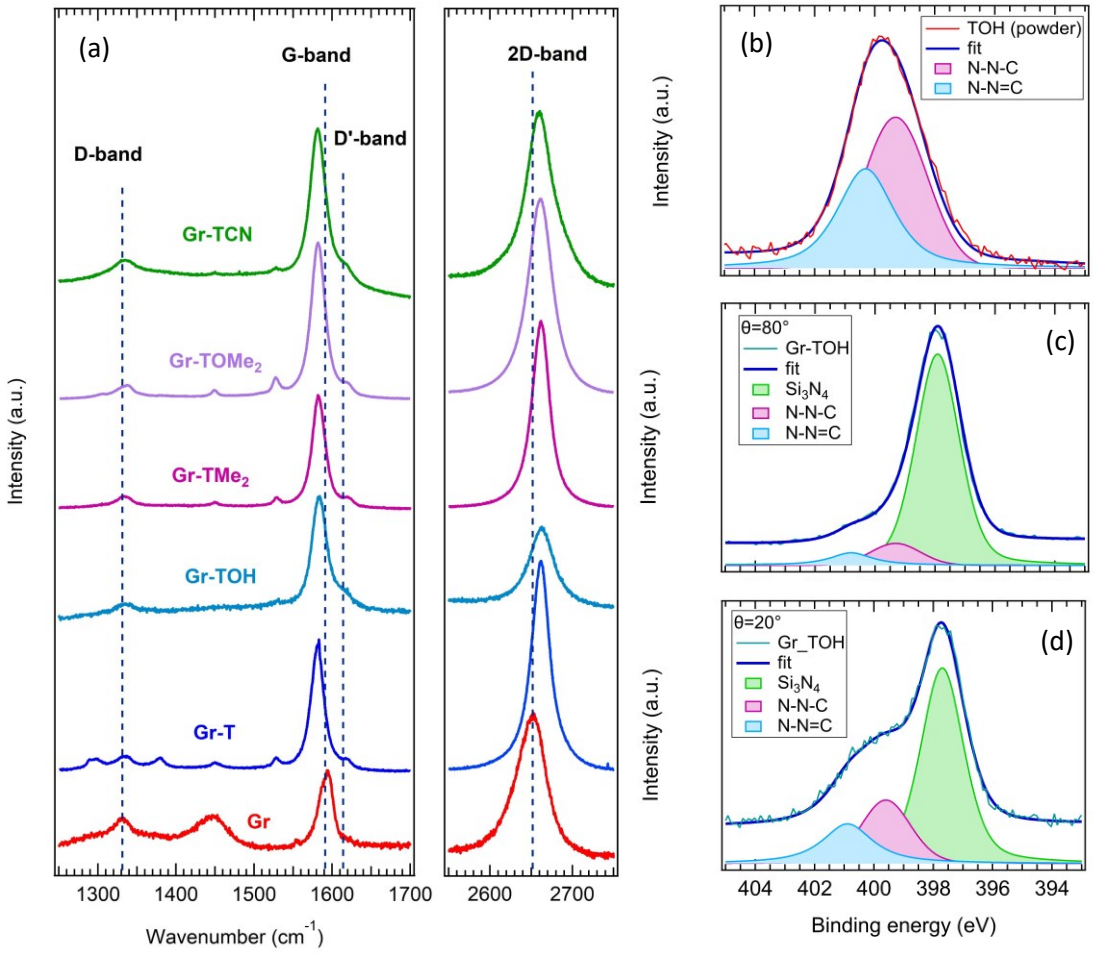

Figure 5: Representative Raman spectra of the pristine graphene (red curve) and the functionalized graphene layers. The D-band is slightly present in all the spectra, confirming the low efficiency of the grafting mechanism. (a) N 1s XPS core level spectra and fitting with Voigt functions ascribed to the N-N-C, N-N=C and Si_3N_4 bonds. Data collected on T-OH annealed powder dropcasted on graphene on Si/SiO_2 substrate (b) and collected on the Gr-TOH sample, at two angular resolutions, nearly normal to the surface, $\theta = 80°$ (c) and nearly grazing to surface, $\theta = 20°$ (d).

Figures 5c and 5d show the N 1s core level spectrum of the Gr-TOH sample, acquired at two different electron take-off angles, i.e., nearly normal to the surface at $\theta = 80°$, and nearly grazing to the surface at $\theta = 20°$. Both spectra could be interpolated with three Voigt functions: two peaks have already been observed in the TOH powder sample and are ascribed to N-N-C (BE = 399.5 eV) and N-N=C (BE = 401 eV) bonds, while the third peak at BE = 397.6 eV is related to

the silicon nitride contribution coming from the substrate.[46] It is clear that in the surface sensitive grazing-angle geometry (i.e. θ = 20°), the contribution of the substrate is attenuated in favour of the surface contributions.

The ratio between the N-N-C and the N-N=C intensities is equal to 1.21 ± 0.25, 1.29 ± 0.18 or 1.36 ± 0.22 for the spectra collected on TOH powder, Gr-TOH at θ = 20° and Gr-TOH at θ = 80° respectively, confirming that the dimerization is the dominant process in the thermal annealing, and the contribution of grafting could be neglected.

Gas sensing

Experimental measurements

The platform prepared with the functionalized samples (see Materials and Methods section) was tested for ammonia sensing. As an example of the array response to ammonia, data collected from the sensors upon exposure to 11 ppm of ammonia are reported in Figure 6-left side. All sensors increase their resistance during the exposure, suggesting a p-type doped nature of the layer themselves. Secondly, a quick response is observed for all the sensors, while the extent of response and the recovery time (i.e. evaluated as the time required by the resistance value to fall by 80% with respect to the highest value achieved during the exposure) vary among the sensors. The faster recovery time has always been detected for the Gr-TOH sample, closely followed by Gr-TCN, while the slower recovery has been detected for the Gr sample. For instance, the analysis of the data after exposure to 11 ppm ammonia for 3 minutes resulted in a recovery time of 8 minutes for Gr-TOH and Gr-TCN, 21 minutes for Gr-T, 22 minutes for Gr-TOMe$_2$, 25 minutes for Gr-TMe$_2$ and more than 1 hour for the Gr sample.

Several exposures at different concentrations have been carried out, in order to draw the calibration curves of all the samples. It is worth to mention, that also the sub-ppm range of ammonia concentration has been explored, and the lowest tested concentration (0.19 ppm) leads to a clear response for Gr, Gr-TCN, Gr-TOH and Gr-TOMe$_2$. Regarding the Gr-T and Gr-TMe$_2$ samples, the experimental limit of detection has been observed to be at 1 ppm for Gr-T, while Gr-TMe$_2$ presented a limit of detection of 0.3 ppm.

Considering the calibration curves, reported in Figure 6–right panel, it is clear that all the functionalized samples show a higher response to ammonia than the pristine one, in particular

the response of Gr-T, Gr-TOH and Gr-TCN is one order of magnitude higher than that of the pristine graphene.

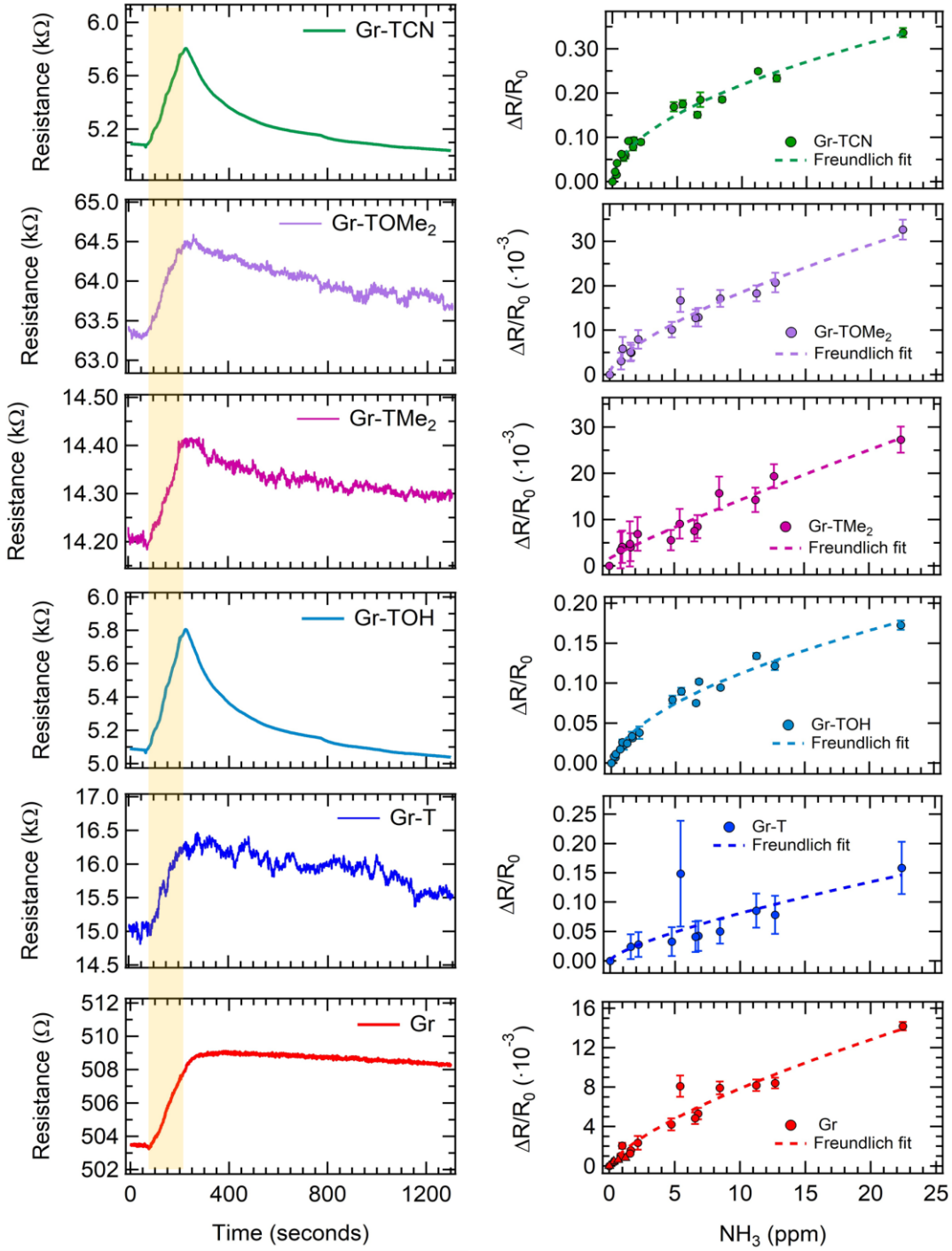

Figure 6: right side: Response of the 6 Gr-based sensor array to 11 ppm ammonia. The shaded area denotes the exposure time. Left side: Calibration curves extracted from several measurements upon ammonia exposures. Error bars are estimated based on the signal-to-noise ratio. Concentration range: 0-23 ppm. Please note that Gr-T and Gr-TOMe$_2$ curves present less data points, since they do not respond in the sub-ppm range.

All the sensors present a nonlinear behaviour, which is quite common in the field of gas sensing with carbon-based materials. The Freundlich isotherm ($\Delta R/R_0 = A[NH_3]^{pow}$) has been used to fit the data (fit parameters reported in Table S1). The fitting parameters (A and pow) have been used to calculate the theoretical detection limit (dl) (see also Table S1), according to the formula: $5\sigma/R_0=A[dl]^{pow}$, where σ is the fluctuation of the electrical signal; Gr-TOH and Gr-TCNT show the best detection limit: 1.5 ppb and 4.2 ppb, respectively.

The data used to build the calibration curves have been also used to perform a benchmarking for the sensitivity (S) parameter, defined as $S= (\Delta R/R_0 \times 100)/[NH_3]$, with respect to literature data on graphene-based sensors. In particular, only papers clearly reporting gas concentration and sensor response/sensitivity, operating at room temperature and in a chemiresistor configuration have been taken into account for this benchmarking.

The comparison, reported in Figure 7, shows that the data obtained in the present work are quite remarkable in terms of sensitivity for Gr-TCN and Gr-TO, while for the other sensors the performances are in line with the reported literature results.[47-59] It is worth pointing out that the 10-1000 ppm is the most tested concentration range for ammonia in literature, while real applications of gas sensors in environmental monitoring, food quality tracking or medical campaigns require sensors able to detect concentration in the low ppm-sub ppm range, where the sensors presented in this work clearly show remarkable performances.

Considering all the sensing parameters, i.e. sensor response, recovery time, detection limit, and sensitivity, it is possible to conclude that the functionalization enhances the sensing capability of the pristine graphene layer, especially in the case of TOH and TCN molecules.

Finally, selectivity in air has been checked by exposing all sensors to different gases at higher concentrations than the one selected for ammonia (i.e. 20 ppm for ammonia and around 100 ppm for the other gases). As shown in the SI (Figure S2), the sensor response to acetone, water, and ethanol molecules is basically negligible, as compared to the response to ammonia for all the tested samples.

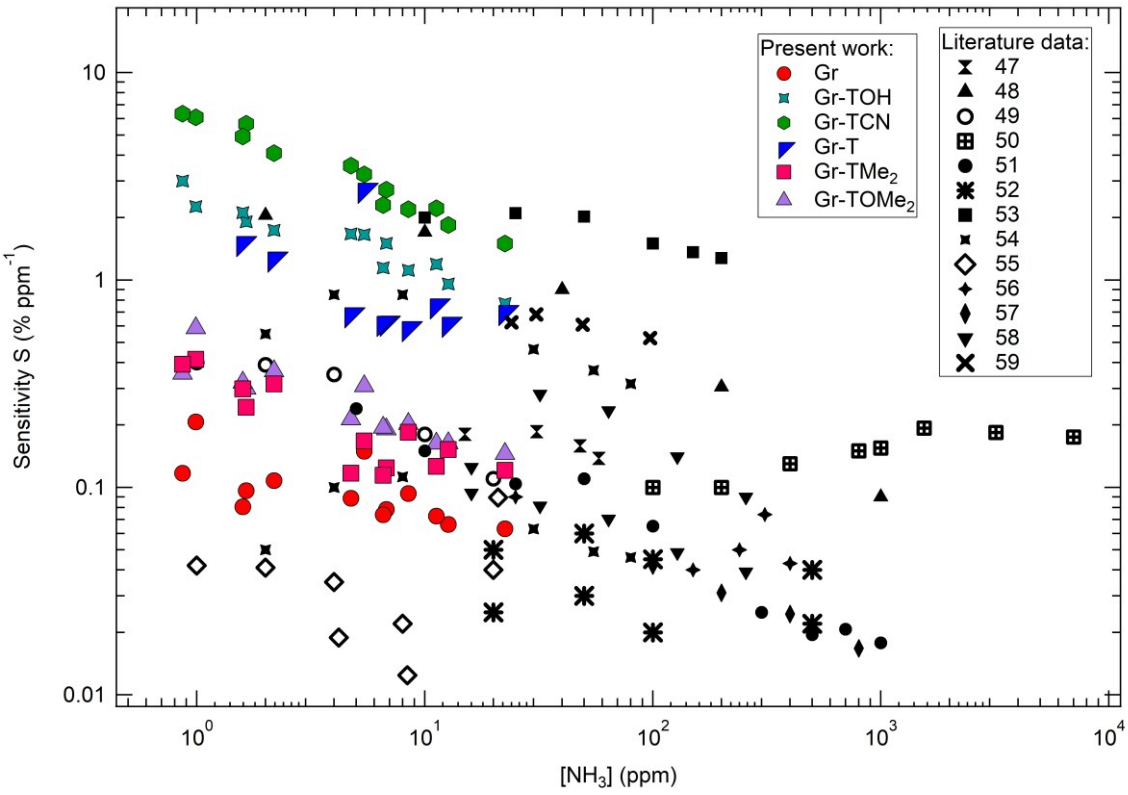

Figure 7: Benchmarking for the sensitivity parameter of the prepared samples with respect to graphene-based chemiresistor performances reported in literature [47-59] for ammonia exposures.

Computational analysis

As pointed out in the previous section, exposure to ammonia leads to an increase in the resistance of the graphene-based sensors. In other words, since graphene is the conductive part of the device, the presence of ammonia must somehow alter its electronic properties. In order to understand this effect, it is necessary to define first what type of interaction is established between the two components of the interface (before exposure to ammonia): 1) the tetrazine molecule and 2) the graphene layer.

As discussed above, the analysis was carried out on the system functionalized with TOH (Gr-TOH), due to its high sensing capability and easier experimental characterization. The Total (TDOS) and Projected (PDOS) Density of States of the Gr-TOH system are reported in Figure 8a. We can observe that the Dirac cone of Gr is preserved (blue curve), indicating a weak interaction with the adsorbed molecule. However, the Dirac point is upshifted with respect to the Fermi level, because of the p-doping character of Gr. Regarding the states of the tetrazine

molecule (red curve), all peaks appear as quite sharp indicating no significant mixing with graphene states. Thus, we consider the molecule as mostly physisorbed on the graphene surface, although in Figure 8a and b we can identify a little coupling in terms of very small bumps in the blue line at the energy position of the molecular peaks. This is also confirmed by the calculated adsorption energy of TOH on Gr of -1.6 eV, which is modest considering the large molecule size.

Nevertheless, not only van-der-Waals (vdW) interactions occur at the interface but also a significant electron transfer from the molecule to graphene is observed (Figure 8b and c). Indeed, we notice how the Dirac point is relatively downshifted with respect to the pristine Gr system, indicating a filling of the empty states: in other words, Gr-TOH is less p-type doped than Gr. From the quantitative point of view, based on the Löwdin population analysis, T-OH is transferring ≈ 1.12 e^- to Gr. Such an electron transfer is also evident from Figure 8c, where the electron depletion region is localized on the molecule side of the interface (in blue), whereas some electron accumulation is visible on the graphene side (in yellow). It is worth noting how the electron rearrangement is less pronounced on Gr, due to its metallic nature, whereas the perturbation is more pronounced on the four N atoms of the central six-membered aromatic ring (where the HOMO of the molecule is highly localized, as shown in Figure S3).

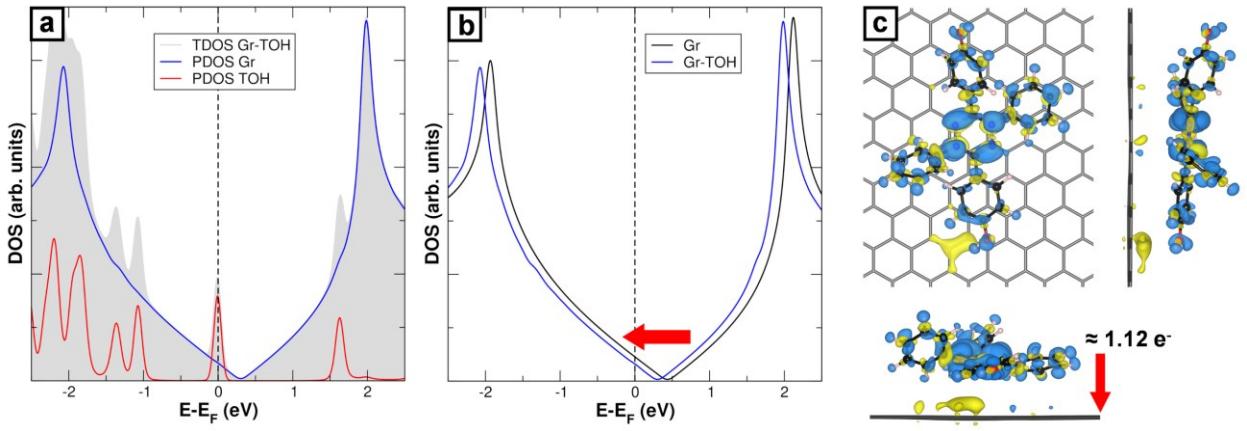

Figure 8: (a) Total (TDOS) and Projected (PDOS) density of states for Gr-TOH. (b) Comparison of the density of states for pristine and tetrazine-functionalized graphene. The Fermi level is scaled to zero and is indicated by a dashed line. (c) Charge density difference plot for the Gr-TOH system. Electron depletion and accumulation are rendered in blue and yellow, respectively (isosurface value is 5×10^{-4} e^- /bohr^3). The red arrow shows the direction of electron charge transfer with the corresponding electrons transferred calculated by using the Löwdin population scheme.

To summarize, vdW dispersion forces and electron charge transfer build up the interaction between T-OH and Gr and will certainly play a role in determining the behavior of adsorbed ammonia. In particular, given the electron-donor properties of ammonia, we expect it will perturbate the TOH and Gr interplay, causing a change in the graphene resistance.

Given the complexity of an accurate experimental determination of the number of NH_3 molecules interacting with Gr-TOH, we have first simulated the presence of one NH_3 molecule per supercell. As shown in Figure 9a, in the most stable configuration, the ammonia molecule interacts with one of the two -OH substituents, forming a strong H-bond leading to an energy gain of -0.61 eV. In the second configuration (Figure 9b), the ammonia molecule is placed on top of the center of the tetrazine ring. Since no H-bond is formed, the adsorption energy is lower by 0.38 eV if compared to the previous case (-0.23 eV).

A second ammonia molecule approaching the system can either adsorb: 1) on the same -OH group interacting with the first NH_3 molecule or 2) on the other free -OH. We did not consider the latter case since we expect a similar binding to that of the first ammonia molecule, i.e. an average adsorption energy of ≈ -0.6 eV. Instead, we considered two NH_3 molecules interacting with the same -OH substituent, as shown in Figure 9c, and the corresponding adsorption energy is -0.40 eV/NH_3.

According to these calculations, we may conclude that the first ammonia molecules tend to interact with the -OH groups by forming H-bonds, rather than interacting directly with the central tetrazine ring of the molecule, which will be accessible at higher coverage.

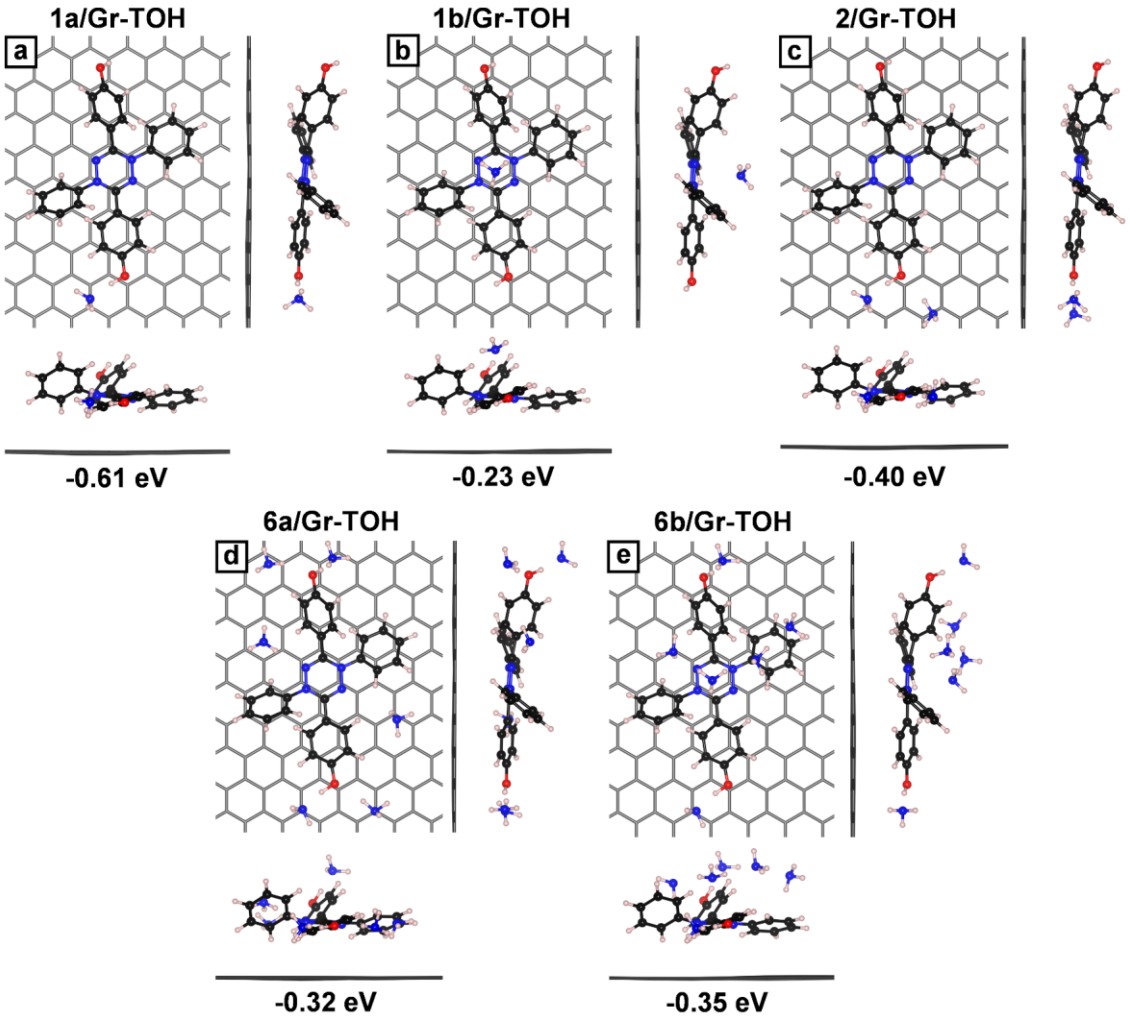

Figure 9: Ball-and-stick models (top and side views) for physisorbed NH_3 on Gr-TOH at different coverages. The corresponding adsorption energies (in eV), normalized per NH_3 molecule, are reported below each panel. Color coding: C atoms in Gr are rendered in dark grey (stick representation); C, N, O, and H atoms in the adsorbed molecules are rendered in black, blue, red, and white, respectively (ball-and-stick representation).

Further simulations along this path (not reported here) show that interaction with the central ring of the tetrazine occurs when six NH_3 molecules approach the tetrazine, which corresponds to a reasonable value matching the experimental condition, i.e. concentration of few ppm (details of this analysis are reported in the S.I. file).

We considered two possible configurations with six ammonia molecules, as reported in Figure 9d and e. In one case, we saturated the -OH groups with four NH_3 molecules, with the remaining two interacting with the central tetrazine ring, while, in the other, we covered the -OH groups with only two molecules, placing the remaining four on the center of the molecule. It is

interesting to note that in this last configuration, one ammonia molecule is set at ≈3 Å above the center of the tetrazine ring, which is the molecular portion that was found to be most involved in the electron transfer between dimer and graphene (see Figure 8c and discussion above). However, both configurations are characterized by a similar adsorption energy of ≈ -0.3 eV.

Once we have investigated structural details and energetics of the system upon NH_3 exposure, we now analyze the effect on the electronic properties of graphene. As mentioned above, the macroscopic effect related to ammonia detection is a change in the graphene resistance, which is related to the occupation of its electronic states. Given the weak interaction between Gr and TOH, we already observed above that the Dirac cone is preserved, which makes monitoring any possible perturbation (in terms of electron charge transfer) caused by the presence of adsorbed ammonia molecules easier: i.e. any significant change in the graphene electronic structure must reflect in a change of the details of the graphene density of states.

The Projected (PDOS) Density of States on Gr states for all the considered models presenting adsorbed NH_3 on the top of Gr-TOH, as well as those without NH_3 for comparison, are reported in Figure 10.

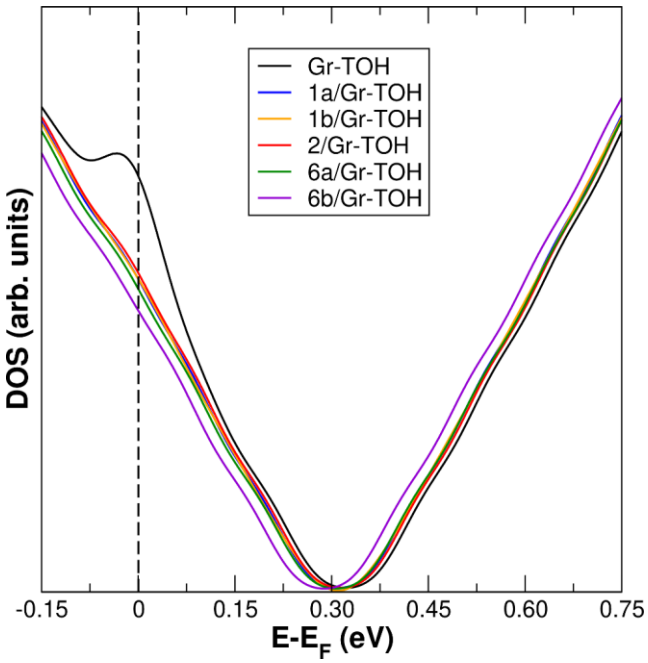

Figure 10: Comparison of projected (PDOS) density of states on Gr for Gr-TOH with and without adsorbed NH_3 molecules. The Fermi level is scaled to zero and indicated by a dashed line.

We can notice that for most of the configurations the position in energy of the Dirac point does not change except for one case: 6b/Gr-TOH, where the shift is of ≈ 20 meV, Besides, the shift direction is in agreement with the experimental observation of an increase in the graphene resistance: the Dirac point is indeed downshifted with respect to Fermi, indicating a filling of graphene empty states. This leads to partial saturation of holes, which are the majority carriers in this system. We have also tested the convergence of the shift value by increasing the density of the K-point mesh used for the calculations, which is one of the most important parameters for an accurate evaluation of the position of the Dirac cone. The results are shown in Figure S4 and prove that, although there are some small differences in the numbers, the observed trend is robust: adsorption of a sufficiently large number of ammonia molecules on the proper adsorption sites makes graphene less p-type doped, reducing the number of hole and thus the number of carriers.

Sensing mechanism

As pointed out in the previous section, the presence of a sufficient amount of ammonia is capable of changing the electronic interplay between Gr and TOH, which is reflected in the position of the graphene Dirac cone. A detailed knowledge of the mechanism underlying the sensing activity is critical to control and properly engineer these systems to achieve high efficiency. Therefore, in this last section, based on our study above, we propose a mechanism for ammonia sensing, highlighting the key factors that are responsible for the high sensitivity of the systems investigated in this study.

The two components of the interface are weakly interacting, as demonstrated by an almost intact graphene Dirac cone. This allows us to study some properties of the two interface components separately. Although a negligible mixing between Gr and TOH states takes place, a significant electron charge transfer from the physisorbed TOH to Gr is registered. The driving force behind this electron transfer is the position of the HOMO of the molecule relative to the Fermi energy of graphene, as shown in Figure 11a.

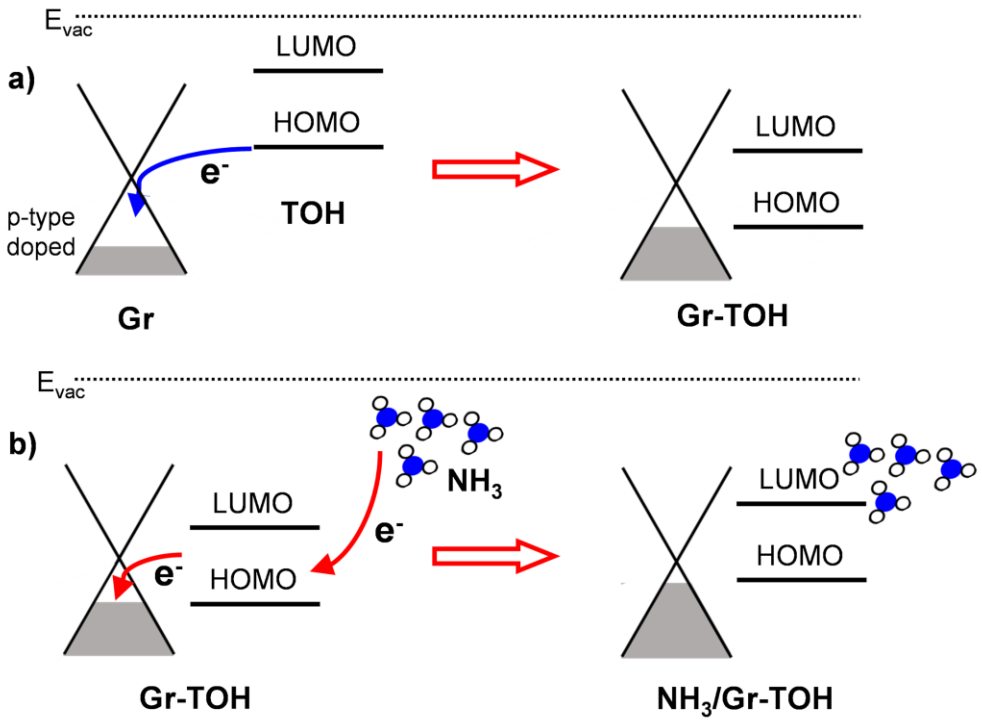

Figure 11: Schematic representation of the interface energy level alignment between TOH and Gr (a) before and (b) after NH_3 exposure. Ammonia molecules are represented with blue (N) and white (H) spheres. Filled states of Gr are shown in grey, whereas empty states are shown in white.

Indeed, the two portions of the system differ in terms of calculated work function (Φ): 3.95 and 5.73 eV for TOH and Gr, respectively. This means that the HOMO of the molecule is at a higher energy with respect to the Fermi of Gr (see Figure S5 for the interface energy level alignment), and when the two systems are brought into contact with each other, electrons flow from the phyisisorbed TOH to Gr in order to align the respective states (with a resulting work function of 5.34 eV for the entire system).

The next question is: what happens when the sample is exposed to NH_3 gas? Ammonia molecules will tend to aggregate in the proximity of physisorbed TOH molecules, initially forming H-bonds with the -OH substituents, and, subsequently, at higher coverages, also interacting with the tetrazine central ring, whose atoms are mostly involved in the HOMO and LUMO of TOH, as shown in Figure S3. As a result of this last interaction, electrons will be flowing from NH_3 to the Gr empty states through the frontier orbitals of TOH, thanks to Gr-TOH coupling, as shown in Figure 8a and Figure 11b. Because of this electron transfer, we expect a reduction of the number of holes present in Gr upon ammonia adsorption.

In this framework, the tetrazine molecule (TOH) has a dual role in the sensing mechanism: (1) it acts as an ammonia concentrator and (2) mediates the electron transfer between ammonia and graphene. Indeed, NH_3 adsorption on pristine Gr is significantly weaker than on Gr-TOH: ≈ 40 meV/NH_3 (in good agreement with the literature [26]) instead of ≈ 200/600 meV/NH_3. Due to this, it is not likely to observe ammonia molecules aggregation on the Gr surface, but they will tend to disperse uniformly on the surface. While in the presence of TOH, ammonia is much more likely to concentrate on the physisorbed molecule, allowing to reach higher local coverages.
However, the effect of TOH is not only to accumulate more ammonia molecules, but also to mediate the electron transfer between ammonia and graphene: in fact, NH_3 molecules transfer electrons to TOH, and, consequently, inducing an electron transfer from TOH to graphene, making it less p-type doped (i.e. increasing its resistance).

Finally, it is worth investigating how different substituents on the phenyl ring of the physisorbed molecule may affect the sensitivity of the system. In this regard, we have performed additional calculations to compare Gr-TOH with Gr-TCN and with Gr-T (as the reference without substituent). The density of states of the gas-phase TOH, TCN, and T molecules is shown in Figure S6a, together with that of p-doped Gr with a common zero reference, i.e. the vacuum level. We clearly note that a different functional group on the phenyl ring changes the position of the molecular levels, in particular the HOMOs: in the case of T, the HOMO is 1.6 eV above the Fermi level of p-doped Gr, whereas for TCN, due to the electron-withdrawing character of the CN group, it is only about 1 eV and for TOH, due to the electron-donating character of the OH group, it is 1.7 eV above the Fermi level of p-doped Gr. Therefore, in all three cases, upon deposition, an electron charge transfer from the molecule to the p-doped Gr is registered, but the entity of such charge transfer will depend on the HOMO position. Quantitatively, the number of transferred electrons, which have the effect to quench part of the holes present in p-doped Gr, is 0.77, 0.49 and 1.12 e^- from T, TCN and TOH, respectively. Consequently, the reduction of the number of holes is the highest for Gr-TOH > Gr-T > Gr-TCN (see the comparison of the Dirac point position shown in Figure S6b). On this basis and given the donating nature of ammonia, Gr-TCN is expected to be the most sensitive for its detection, in perfect agreement with experiments (Figure 7).

In addition to the density of charge carriers, transport properties also depend on the mobility of charge carriers. As recognized by Gosling et al., [60] mobility in graphene can directly influence electrical conductivity and its dependence on carrier density. In this frame, mobility and charge density appear to be intertwined, though an assessment of their relationship still represents a challenging task that can be properly addressed by considering experimental data and simulations from GFET devices.[60-62] In our study, we did not access the information provided by a GFET readout, as our devices are operated on the basis of chemiresistor read-out scheme (i.e. without a gate). For this reason, we specifically address the change in electron density, but we are aware that mobility decrease cannot be neglected as an effect leading to the resistivity increase observed in functionalized samples with respect to the pristine one. This decrease is already observed before exposure to ammonia, suggesting that the deposition of the tetrazole layer can itself decrease the mobility of electrons in graphene. As recognized in Ref. 60, the properties of graphene heterostructures can be affected by both the unintentional presence of charge impurities in the vicinity of the graphene layer and those deliberately introduced by the top layer in Gr heterostructures, as a result of Gr decoration with different systems, from 0D to 2D. Indeed, spatial inhomogeneity in the impurity potential may result in a broadening of the energy distribution of charge carries (electron and holes) near the Fermi level (Dirac cone), ultimately determining a mobility decrease.

Conclusions

In this work an easy and cost-effective method to functionalize graphene for activating its ammonia sensitivity has been presented. Tetrazoles, which can dimerize in tetrazine upon thermal treatment, have been selected as the precursor molecules for functionalization. At first, DFT calculations have demonstrated that, during the thermal treatment, the dimerization process is energetically more favorable than covalent grafting, consistently with the experimental results obtained from Raman spectroscopy. Since both this type of functionalization method and the use of tetrazoles have never been considered before to prepare graphene-based chemiresistors, this represents a promising approach to develop graphene-based sensing platforms. The test on the sensing performances clearly shows a remarkable sensitivity to ammonia, extending the current range of ammonia detection with graphene-based chemiresistor down to the sub-ppm range, as

results from a benchmarking with data available in the literature. Wi the help of DFT calculations we have identified the mechanism of sensing and disclosed a dual role played by the tetrazine molecules (TOH), as (i) they act as an ammonia concentrator and (ii) also mediate the electron transfer between ammonia and graphene.

Material and Methods

Synthesis

Details of synthetic procedures and characterization of prepared compounds are presented in the Supporting information.

Samples preparation

Selected 2,5-diaryltetrazole (**1**-**5**) was dissolved in CH_2Cl_2 at a concentration of 5 μg/mL. The prepared solutions have been drop casted (15 drops) on graphene on silicon nitride layers (1x1 cm^2, purchased by Graphenea) with a standard glass pasteur pipet. After complete solvent evaporation (10 min), the samples have been heated at 250 °C for 1 h in a sealed glass oven (Buchi Glass Oven B-585), under nitrogen atmosphere. After cooling to RT maintaining the nitrogen atmosphere, the samples have been removed from the oven and gently washed with CH_2Cl_2 (≈ 2 mL).

Sample characterization

Raman spectroscopy, atomic force microscopy (AFM) and X-ray photoemission spectroscopy (XPS) measurements has been performed to characterize the samples.

Raman spectra have been collected on a CGS device with a Renishaw-Invia system, equipped with a 633 nm laser source. The laser light has been always focused onto the sample with a 100X objective. An 1800 lines/mm grating and a laser power of 5 mW have been used for the measurements.

AFM images have been acquired with a Park NX 10 AFM system in non-contact mode in air-solid interface with a tip operating at a resonance frequency of about 300 kHz. All the images processing has been performed using the Gwyddion software.

XPS data have been collected by using the Al Kα line (hν = 1486.6 eV) from a twin anode x-ray source and a fully calibrated VG-Scienta R3000 spectrometer, with an overall resolution of 0.9 eV. [63]

Gas exposures

Electrical contacts made of silver paint have been printed as small stripes at the opposite sides of a pristine sample and on the 5 functionalized layers. All samples have then been mounted on a properly designed platform (Figure S7a), able to host up to 8 sensors, which work simultaneously. The present platform allows a direct comparison of the behaviour of the sensors under the same environmental conditions. Two commercial sensors have been put on the platform: a relative humidity (RH) sensor (humidity sensor HIH-4000 series - Honeywell Sensing) and a temperature sensor (Thermistor NTC PCB 5K - Murata).

Gas exposure has been carried out at room temperature in a sealed chamber, by introducing a mixture of synthetic air with a selected concentration of the analyte. Two cylinders have been used to feed the chamber through programmable mass-flow controllers operating in a 20-500 sccm range. The first cylinder (S.I.A.D. Spa) was loaded with 47 ppm of ammonia in synthetic air, while the second was loaded with synthetic air alone (S.I.A.D. Spa) and used to change the overall concentration of ammonia in the chamber. Gas from both cylinders was pre-mixed before entering the chamber. The analyte concentration has been determined by a calibrated sensor (Figaro, Mod. TGS 2602), while temperature and R.H. values have been monitored by two sensors, above mentioned, placed on the same board hosting the sensor array. During measurements the overall R.H was (50 ± 10) %. Exposure time was set to 3 minutes and after each exposure the chamber has been purged by flushing the chamber with synthetic air until the initial resistance value of the sensors has been restored.

The developed graphene-based sensors work in a chemiresistor configuration: the gas analytes are detected by measuring the resistance changes of the sensing layers induced by the interaction with the gas molecules and the electronic circuit of each sensor is reported in Figure S7b. A load resistor (R_L) is in series with the sensor and, applying a constant voltage and monitoring the output voltage (V_{OUT}) across the sample, it is possible to track the resistance R of the sensor. The response of the sensor is then defined as $\Delta R/R_0 = (R-R_0)/R_0$, where R_0 is the baseline sensor resistance before the gas exposure, and $\Delta R = R-R_0$ is the resistance variation due to the interaction with the gas molecules. Figure S7c shows a schematic typical change in a graphene-based sensor resistance during an ammonia exposure and how ΔR, R, and R_0 are obtained. Ammonia, being a reducing gas, when interacting with a p-type doped graphene can donate electrons to the layer, saturating the holes (majority carriers) and therefore an increase of the

resistance is observed. Considering several exposures, calibration curves for each sensor could be obtained by plotting the sensor response $\Delta R/R_0$ versus the gas concentration.

Computational details

Density functional theory (DFT) calculations have been performed using the plane-wave-based Quantum ESPRESSO package (QE). [64,65] The ultrasoft pseudopotentials [66,67] have been adopted to describe the electron-ion interactions with C (2s, 2p), O (2s, 2p), N (2s, 2p), and H (1s) treated as valence electrons. Energy cutoffs of 46 and 326 Ry (for kinetic energy and charge density expansion, respectively) have been adopted for all calculations. The convergence criterion of 0.026 eV/Å for the forces has been used during geometry optimization, and the convergence criterion for the total energy has been set at 10^{-6} Ry. To properly take into account weak interactions, the van der Waals density functional vdW-DF2^{C09x} has been used, [68,69] as implemented in the QE code.

To model graphene, an ($8 \times 6\sqrt{3}$) supercell, containing 192 C atoms, has been adopted. The Gr surface area available in our model is 5.05 nm^2. A Monkhorst-Pack [70] *k*-Points mesh of $6 \times 4 \times 1$ and $18 \times 12 \times 1$ was used for the geometry relaxation and density of states (DOS) evaluation, respectively. Denser *k*-Points meshes of $9 \times 6 \times 1$ and $27 \times 18 \times 1$ (single point calculation and DOS, respectively) have been tested for specific configurations, as indicated in the next section. To avoid interactions between adjacent periodic images, a vacuum space of 25 Å has been included in the supercell model.

All calculations involving graphene have been charged by removing one electron from the cell, in order to simulate the p-doped nature of the experimental graphene samples.

Associated Content

Supporting Information

The Supporting Information is available free of charge on the ACS Publications website at DOI:

Notes

The authors declare no competing financial interest.

Acknowledgements

This work has been supported by the project "MADAM - Metal Activated 2D cArbon-based platforMs" funded by the MIUR Progetti di Ricerca di Rilevante Interesse Nazionale (PRIN) Bando 2017 - grant 2017NYPHN8. S.F. and D.P. equally contributed to this work.

Reference

1 Agrawal, A. V., Kumar, N., Kumar, M. Strategy and Future Prospects to Develop Room-Temperature-Recoverable NO 2 Gas Sensor Based on Two-Dimensional Molybdenum Disulfide. *Nano-micro letters* **2021**, *13*(1), 1-58.

2 Nayyar, A.; Puri, V.; Le, D. N. A Comprehensive Review of Semiconductor-Type Gas Sensors for Environmental Monitoring. *Rev. Comput. Eng. Res.* **2016**, *3*(3), 55-64.

3 Freddi, S.; Drera, G.; Pagliara, S.; Goldoni, A.; Sangaletti, L. Enhanced selectivity of target gas molecules through a minimal array of gas sensors based on nanoparticle decorated SWCNTs. *Analyst* **2019**, *144* (13), 4100-4110.

4 Pereira, P.F.M.; de Sousa Picciani, P. H.; Calado, V.; Tonon, R. V. Electrical gas sensors for meat freshness assessment and quality monitoring: A review. *Trends Food Sci Technol*. **2021**, *118*, 36–44

5 Jiang, S.; Liu, Y. Gas sensors for volatile compounds analysis in muscle foods: A review. *Trends Anal. Chem.* **2020**, *126*, 115877.

6 Barreca, D.; Gasparotto, A.; Gri, F.; Comini, E.; Maccato, C. Plasma-Assisted Growth of β-MnO2 Nanosystems as Gas Sensors for Safety and Food Industry Applications. *Adv. Mater. Interfaces* **2018**, *5*, 1800792.

7 Marzorati, D.; Mainardi, L.; Sedda, G.; Gasparri, R.; Spaggiari, L.; Cerveri, P. MOS Sensors Array for the Discrimination of Lung Cancer and At-Risk Subjects with Exhaled Breath Analysis. *Chemosensors* **2021**, *9*, 209.

8 Freddi, S.; Emelianov, A. V.; Bobrinetskiy, I. I.; Drera, G.; Pagliara, S.; Kopylova, D. S.; Chiesa, M.; Santini, G.; Mores, N.; Moscato, U.; Nasibulin, A. G.; Montuschi, P.; Sangaletti, L. Development of a Sensing Array for Human Breath Analysis Based on

SWCNT Layers Functionalized with Semiconductor Organic Molecules. *Adv Health Mat* **2020**, *9*(12), 2000377.

9 Zhou, X.; Xue, Z.; Chen, X.; Huang, C.; Bai, W.; Luc, Z.; Wang, T. Nanomaterial-based gas sensors used for breath diagnosis. *J. Mater. Chem. B* **2020**, *8*, 3231-3248.

10 Drera, G.; Freddi, S.; Emelianov, A. V.; Bobrinetskiy, I. I.; Chiesa, M.; Zanotti, M.; Pagliara, S.; Fedorov, F.; Nasibulin, A. G.; Montuschi, P.; Sangaletti, L. Exploring the performance of a functionalized CNT-based sensor array for breathomics through clustering and classification algorithms: from gas sensing of selective biomarkers to discrimination of chronic obstructive pulmonary disease. *RSC Adv.* **2021**, *11*, 30270-30282.

11 Chuang, M.-Y.; Chen, C. C.; Zan, H.-W.; Meng, H.-F.; Lu, C.-J. Organic gas sensor with an improved lifetime for detecting breath ammonia in hemodialysis patients. ACS Sens. 2017, 2, 1788.

12 Kirkby, J. ; Curtius, J. ; Almeida, J. et al. Role of sulphuric acid, ammonia and galactic cosmic rays in atmospheric aerosol nucleation. *Nature* **2011**, *476*, 429–433.

13 Nguyen, L.H.; Naficy, S.; McConchie, R.; Dehghani, F.; Chandrawati, R. Polydiacetylene-based sensors to detect food spoilage at low temperatures. *J. Mater. Chem. C* **2019**, *7*, 1919.

14 Bogue, R. Nanomaterials for gas sensing: a review of recent research. *Sensor Rev.***2014**, *34*(1), 1–8.

15 Wang, T., Huang, D., Yang, Z. et al. A Review on Graphene-Based Gas/Vapor Sensors with Unique Properties and Potential Applications. *Nano-Micro Lett.* **2016,** *8*, 95–119.

16 Varghese, S. S.; Lonkar, S.; Singh, K.K.; Swaminathan, S.; Abdala, A. *Sens. Actuators B* **2015**, *218*, 160–183.

17 Toda, K.; Furue, R.; Hayami, S. Recent progress in applications of graphene oxide for gas sensing: A review. *Analytica Chimica Acta* **2015**, *878*, 43–53.

18 Tian, W.; Liu, X.; Yu, W. Research progress of gas sensor based on graphene and its derivatives: a review. *Applied Sciences* **2018**, *8*(7), 1118.

19 Tan, R. K. L.; Reeves, S.P.; Hashemi, N.; Thomas, D.G.; Kavak, E.; Montazami, R.; Hashemi, N.N. Graphene as a flexible electrode: review of fabrication approaches. *J. Mater. Chem. A* **2017**, *5*, 17777–17803.

20 Choi, Y.R.; Yoon, Y.-G.; Choi, K.S.; Kang, J.H.; Shim, Y.S.; Kim, Y.H.; Chang, H.J.; Lee, J.-H.; Park, C.R.; Kim, S.Y.; Jang, H. W. Role of oxygen functional groups in graphene oxide for reversible room-temperature NO_2 sensing. *Carbon* **2015**, *91*, 178–187.

21 Tang, X., Debliquy, M., Lahem, D., Yan, Y., & Raskin, J. P. (2021). A Review on Functionalized Graphene Sensors for Detection of Ammonia. Sensors, 21(4), 1443.

22 Alzate-Carvajal, N.; Luican-Mayer, A. Functionalized Graphene Surfaces for Selective Gas Sensing. *ACS omega* **2020**, *5*(34), 21320-21329.

23 Georgakilas, V.; Otyepka, M.; A.B.; Chandra, V.; Kim, M.; Kemp, K.C.; Hobza, P.; Zboril, R.; Kim, K.S. Functionalization of Graphene: Covalent and Non-Covalent Approaches, Derivatives and Applications. *Chem. Rev.* **2012**, *112*, 6156−6214.

24 Guo, B.; Fang, L.; Zhang, B.; Gong, J. R. Graphene Doping: A Review. *Insciences J.* **2011**, *1*(2), 80-89.

25 Wang, H.; Maiyalagan, T.; Wang, X. Review on Recent Progress in Nitrogen-Doped Graphene: Synthesis, Characterization, and Its Potential Applications. *ACS Catal.* **2012**, *2*, 781−794.

26 Zhang, Z.; Zhang, X.; Luo, W.; Yang, H.; He, Y.; Liu, Y.; Zhang, Z.; Peng, G. Study on adsorption and desorption of ammonia on graphene. *Nanoscale Res. Lett.* **2015**, *10(1)*, 1-8.

27 Ghanbari, R.; Safaiee, R.; Sheikhi, M. H.; Golshan, M. M.; Horastani, Z. K. Graphene decorated with silver nanoparticles as a low-temperature methane gas sensor. *ACS applied materials & interfaces* **2019**, *11*(24), 21795-21806.

28 Ambrosio, G.; Brown, A.; Daukiya, L.; Drera, G.; Di Santo, G.; Petaccia, L.; De Feyter, S.; Sangaletti, L.; Pagliara, S. Impact of covalent functionalization by diazonium chemistry on the electronic properties of graphene on SiC. *Nanoscale* **2020**, *12*(16), 9032-9037.

29 Sawada, K.; Tanak, T.; Yokoyama1, T.; Yamachi, R.; Oka, Y.; Chiba, Y.; Masai, H.; Terao, J.; Uchida, K. Co-porphyrin functionalized CVD graphene ammonia sensor with high selectivity to disturbing gases: hydrogen and humidity. *Jpn. J. Appl. Phys.* **2020**, *59*, SGGG09

30 Jamieson, C.; Livingstone, K. The Nitrile Imine 1, 3-Dipole: Properties, Reactivity and Applications. Springer Nature, 2020.

31 Barrejon, M.; Gomez-Escalonilla, M.J.; Fierro, J.L.G.; Prieto, P.; Carrillo, J.R.; Rodrıguez, A.M.; Abellan, G.; Lopez-Escalante, M.C. et al. Modulation of the exfoliated graphene work function through cycloaddition of nitrile imines. *Phys.Chem.Chem.Phys.* **2016**, *18*, 29582.

32 Birkofer, L.; Ritter, A.; Richter, P. Thermolyse silylierter Tetrazole. *Chemische Berichte* **1963**, *96*(10), 2750-2757.

33 Garanti, L.; Sala, A.; Zecchi, G. Intramolecular and intermolecular 1, 3-dipolar cycloadditions of nitrile oxides bearing an alkenyl substituent. *The Journal of Organic Chemistry* **1975**, *40*(16), 2403-2406.

34 Zhang, Y.; Liu, W.; Zhao, Z. K. Nucleophilic trapping nitrilimine generated by photolysis of diaryltetrazole in aqueous phase. *Molecules* **2014**, *19*(1), 306-315.

35 Zhao, S.; Dai, J.; Hu, M.; Liu, C.; Meng, R.; Liu, X.; Wang, C.; Luo, T. Photo-Induced Coupling Reactions of Tetrazoles with Carboxylic Acids in Aqueous Solution: Application in Protein Labelling. *Chem. Commun. (Camb.)* **2016**, *52* (25), 4702–4705.

36 Vaghi, L.; Monti, M.; Marelli, M.; Motto, E.; Papagni, A.; Cipolla, L. Photoinduced Porcine Gelatin Cross-Linking by Homobi- and Homotrifunctional Tetrazoles. *Gels* **2021**, *7* (3), 124.

37 Li, Y.; Zhang, W.; Sun, Z.; Sun, T.; Xie, Z.; Huang, Y.; Jing, X. Light-Induced Synthesis of Cross-Linked Polymers and Their Application in Explosive Detection. *Eur. Polym. J.* **2015**, *63*, 149–155.

38 Dietrich, M.; Delaittre, G.; Blinco, J. P.; Inglis, A. J.; Bruns, M.; Barner-Kowollik, C. Photoclickable Surfaces for Profluorescent Covalent Polymer Coatings. *Adv. Funct. Mater.* **2012**, *22* (2), 304–312.

39 Lesnikovich, A. I.; Levchik, S. V.; Balabanovich, A. I.; Ivashkevich, O. A.; Gaponik, P. N. The Thermal Decomposition of Tetrazoles. *Thermochim. Acta* **1992**, *200*, 427–441.

40 Ito, S.; Tanaka, Y.; Kakehi, A.; Kondo, K.-I. A Facile Synthesis of 2,5-Disubstituted Tetrazoles by the Reaction of Phenylsulfonylhydrazones with Arenediazonium Salts. *Bull. Chem. Soc. Jpn.* **1976**, *49* (7), 1920–1923.

41 Huisgen, R.; Seidel, M.; Sauer, J.; McFarland, J.; Wallbillich, G. Communications: The Formation of Nitrile Imines in the Thermal Breakdown of 2,5-Disubstituted Tetrazoles. *J. Org. Chem.* **1959**, *24* (6), 892–893.

42 Ferrari, A. C.; Basko, D. M. Raman spectroscopy as a versatile tool for studying the properties of graphene, *Nat Nanotechnol* **2013**, *8*, 235–246.

43 Gupta, A.; Chen, G.; Joshi, P.; Tadigadapa, S.; Eklund, P. C. Raman scattering from high-frequency phonons in supported n-graphene layer films, *Nano letters* **2006**, *6*(12), 2667-2673.

44 Jiang, J. Z.; Stahl, K.; Berg, R. W.; Frost, D. J.; Zhou, T. J.; Shi, P. X. Structural characterization of cubic silicon nitride. *EPL* **2000**, *51*, 62.

45 Li, Y.; Alain-Rizzo, V.; Galmiche, L.; Audebert, P.; Miomandre, F.; Louarn, G.; Bozlar, M.; Pope, M. A.; Dabbs, D. M.; Aksay, A. Functionalization of graphene oxide by tetrazine derivatives: a versatile approach toward covalent bridges between graphene sheets. *Chemistry of Materials* **2015**, *27*(12), 4298-4310.

46 Chourasia, A. R., Chopra, D. R. A Study of Si3N4 by XPS. *Surface Science Spectra* **1993**, *2*(2), 117-122.

47 Gautam, M.; Jayatissa, A. H. Ammonia gas sensing behavior of graphene surface decorated with gold nanoparticles. *Solid-State Electronics* **2012**, *78*, 159–165.

48 Javari, F.; Castillo, E.; Gullapalli, H.; Ajayan, P. M.; Koratkar, N. High sensitivity detection of NO2 and NH3 in air using chemical vapor deposition grown graphene. *Appl. Phys. Lett.* **2012**, *100*, 203120.

49 Chen, G.; Paronyan, T. M.; Harutyunyan, A. R. Sub-ppt gas detection with pristine Graphene. *Appl. Phys. Lett.* **2012**, *101*, 053119.

50 Wu, Z.; Chen, X.; Zhu, S.; Zhou, Z.; Yao, Y.; Quan, W.; Liu, B. Enhanced sensitivity of ammonia sensor using graphene/polyaniline nanocomposite. *Sens Actuators B* **2013**, *178*, 485– 493.

51 Seekaew, Y.; Phokharatkul, D.; Wisitsoraat, A.; Wongchoosuk, C. Highly sensitive and selective room-temperature NO2 gas sensor based on bilayer transferred chemical vapor deposited graphene. *Org Electron* **2014**, *15*, 2971–2981.

52 Aziza, Z.B.; Zhang, Q.; Baillargeat, D. Graphene/mica based ammonia gas sensors. *Appl. Phys. Lett.* **2014**, *105*, 254102.

53 Xiang, C.; Jiang, D.; Zoua, Y.; Chu, H.; Qiu, S.; Zhang, H.; Xu, F.; Sun, L.; Zheng, L. Ammonia sensor based on polypyrrole–graphene nanocomposite decorated with titania nanoparticles. *Ceram Int* **2015**, *41*, 6432–6438.

54 Zanjani, S.M.M.; Sadeghi, M.M.; Holt, M.; Chowdhury, S. F.; Tao, L.; Akinwande, D. Enhanced sensitivity of graphene ammonia gas sensors using molecular doping. *Appl. Phys. Lett.* **2016**, *108*, 033106.

55 Lv, R.; Chend, G.; Lie, Q.; McCreary, A.; Botello-Méndez, A.; Morozov, S. V.; Liang, L.; Declerck, X. et al. Ultrasensitive gas detection of large-area boron-doped graphene. *PNAS* **2015**, *112* (47), 14527–14532.

56 Wu, D.; Peng, Q.; Wu, S.; Wang, G.; Deng, L.; Tai, H.; Wang, L.; Yang, Y.; Dong, L.; Zhao, Y.; Zhao, J.; Sun, D.; Lin, L. A Simple Graphene NH3 Gas Sensor via Laser Direct Writing. *Sensors* **2018**, *18*, 4405.

57 Liang, T.; Liu, R.; Lei, C.; Wang, K.; Li, Z.; Li, Y. Preparation and Test of NH3 Gas Sensor Based on Single-Layer Graphene Film. *Micromachines* **2020**, *11*, 965.

58 Srivastava, S.; Jain, S.K.; Gupta, G.; Senguttuvan, T. D.; Gupta, B. K. Boron-doped few-layer graphene nanosheet gas sensor for enhanced ammonia sensing at room temperature, *RSC Adv.* **2020**, *10*, 1007.

59 Zhu, Y.; Yu, L.; Wu, D.; Lv, W.; Wang, L. A high-sensitivity graphene ammonia sensor via aerosol jet printing. *Sens Actuators A* **2021**, *318*, 112434.

60 Gosling, J. H.; Makarovsky, O.; Wang, F.; Cottam, N. D.; Greenaway, M. T.; Patanè, A.; Wildman, R.D.; Tuck, C. J.; Turyanska, L.; Fromhold, T. M. Universal mobility characteristics of graphene originating from charge scattering by ionised impurities. *Commun. Phys.* **2021**, *4*(1), 1-8.

61 Park, J.; Rautela, R.; Alzate-Carvajal, N.; Scarfe, S.; Scarfe, L.; Alarie, L.; Luican-Mayer, A.; Ménard, J. M. UV Illumination as a Method to Improve the Performance of Gas Sensors Based on Graphene Field-Effect Transistors. *ACS sensors* **2021,** *6*(12), 4417-4424.

62 Alzate-Carvajal, N.; Park, J.; Pykal, M.; Lazar, P.; Rautela, R.; Scarfe, S.; Scarfe, L.; Ménard, J. M.; Otyepka, M.; Luican-Mayer, A. Graphene Field Effect Transistors: A Sensitive Platform for Detecting Sarin. *ACS Appl. Mater. Interfaces* **2021***, 13(51),* 61751–61757.

63 Drera, G.; Salvinelli, G.; Åhlund, J.; Karlsson, P. G.; Wannberg, B.; Magnano, E.; Nappini, S.; Sangaletti, L. *J. Electron Spectrosc. Relat. Phenom* **2014,** *195*, 109.

64 Giannozzi, P.; Baroni, S.; Bonini, N.; Calandra, M.; Car, R.; Cavazzoni, C.; Ceresoli, D.; Chiarotti, G. L.; Cococcioni, M.; Dabo, I.; et al. Quantum ESPRESSO: a modular and open-source software project for quantum simulations of materials. *J. Phys.: Condens. Matter* **2009**, *21*, 395502.

65 Giannozzi, P.; Andreussi, O.; Brumme, T.; Bunau, O.; Buongiorno Nardelli, M.; Calandra, M.; Car, R.; Cavazzoni, C.; Ceresoli, D.; Cococcioni, M.; et al. Advanced capabilities for materials modelling with Quantum ESPRESSO. *J. Phys.: Condens. Matter* **2017**, *29*, 465901.

66 Vanderbilt, D. Soft self-consistent pseudopotentials in a generalized eigenvalue formalism. *Phys. Rev. B* **1990**, *41*, 7892.

67 Dal Corso, A. Pseudopotentials periodic table: From H to Pu. *Computational Materials Science*, **2014**, 95, 337-350.

68 Lee, K.; Murray, ÉD.; Kong, L.; Lundqvist, B. I.; Langreth, D. C. Higher-accuracy van der Waals density functional. *Phys. Rev. B: Condens. Matter Mater. Phys*. **2010**, *82*, 081101.

69 Hamada, I.; Otani, M. Comparative van der Waals density-functional study of graphene on metal surfaces. *Phys. Rev. B: Condens. Matter Mater. Phys.* **2010**, *82*, 153412.

70 Monkhorst, H. J.; Pack, J. D. Special points for Brillouin-zone integrations. *Phys. Rev. B: Condens. Matter Mater. Phys.* **1976**, *13*, 5188.

Table of Contents